www.sciencemag.org/content/346/6213/1100/suppl/DC1

Supplementary Materials for

Discovery of bridgmanite, the most abundant mineral in Earth, in a shocked meteorite

Oliver Tschauner,* Chi Ma, John R. Beckett, Clemens Prescher, Vitali B. Prakapenka, George R. Rossman

*Corresponding author. E-mail: olivert@physics.unlv.edu

Published 28 November 2014, *Science* **346**, 1100 (2014)
DOI: 10.1126/science.1259369

This PDF file includes:

Materials and Methods
Figs. S1 to S6
Tables S1 and S2
Caption for Data table S1
References

Other Supporting Online Material for this manuscript includes the following:
(available at www.sciencemag.org/content/346/6213/1100/suppl/DC1)

Data table S1: Bridgmanite_hkl .xls file
Data table S2: Bridgmanite .cif file

Materials and Methods

Material

The type bridgmanite material in Caltech Tenham section TB-MC2L (Figs. S1,S4,S5) is deposited in the collections of the Smithsonian Institution's National Museum of Natural History, Washington DC, USA, with registration number USNM 7703.

Structural characterization

Diffraction data were collected at the undulator beamline 13-IDD (GSECARS, APS, Argonne National Laboratory) using a primary beam energy of 37.077 keV (λ = 0.3344Å) monochromatized by a double crystal Si (111) monochromator. The X-ray beam was focused to ~3×4 μm^2 by vertical and horizontal Kirkpatrick-Baesz mirrors of 200 mm focal length and a MAR165 CCD detector was used for collecting diffraction data. The thin section containing bridgmanite was scanned in 4 μm steps horizontally and vertically via the focused X-ray beam over the selected region of a shock-melt vein (Fig. S4). Diffraction patterns were recorded in transmission geometry at each step. The diffraction pattern images were corrected for diffuse scattering from the glass slide of the thin section using Fit2D (*32*). The patterns were then corrected for geometric distortion from detector tilt using GSE-ADA (*33*) and integrated using Fit2D (*32*). The low abundance of bridgmanite and partial overlap with reflections from other minerals made the analysis extremely tedious: We acquired a total of 4000 diffraction images and selected 200 for manual examination. We observed bridgmanite only in association with

akimotoite and only in pseudomorphosis after small (20-50 μm edge length) orthopyroxene crystals that had been entrained by the shock melt.

Bridgmanite was observed at several locations in USNM 7703 as a minor phase. We selected a pattern for detailed structure analysis that had a comparatively large phase fraction of bridgmanite with relatively low overlap of reflections due to diffraction from other, more dominant phases and cross-checked with other patterns using the same analysis methods. Rietveld refinements of the bridgmanite structure were conducted with Powdercell (*34*) using Pseudo-Voigt profiles with the following final parameters: U = 0.114, V = 0.011, V = 0.012, fixed mixing parameters $n_a = 0.5$ and $n_b = 0.0$, and a scale factor of 0.14. Rietveld refinement converged to an R_{wp} of 0.08 with a $R_{exp} = 0.03$. There were 799 observations and the χ^2 was 1.96. However, the contribution of bridgmanite to the Rietveld refinement in this and similar patterns was only ~11% (Fig. 1) and there was still overlap of reflections with diffraction from coexisting ringwoodite and akimotoite. We, therefore, made a LeBail extraction of structure factor moduli ($R_p = 0.06$, Fig. 2) and conducted a reversed Monte Carlo global optimization (*35*) based on the extracted |F(hkl)|, which converged to a R_{Bragg} of 0.15 (Table S2). These results confirm that bridgmanite is an orthorhombic ABO_3-perovskite and not an artifact of profile fitting the coexisting akimotoite and ringwoodite. Atom coordinates and unit cell dimensions are given in Table S3.

Electron back-scatter diffraction (EBSD) analysis of individual bridgmanite crystals (using a HKL EBSD system on a ZEISS 1550VP FE-SEM at Caltech) was unsuccessful due to fast beam damage so that, no pattern could be obtained. Although bridgmanite became amorphous under the e-beam, there was the contrast in backscatter

electron (BSE) images with the distinctive appearance of crystallites to allow us to readily distinguish between crystallites of bridgmanite and akimotoite and the host glass (Figs. 1 and S1). In addition, akimotoite was identified within these aggregates by EBSD patterns.

Chemical analysis

Quantitative elemental microanalyses of the type material were carried out at Caltech using a JEOL 8200 electron microprobe operated at 15 kV and 10 nA in focused beam mode and processed with the CITZAF correction procedure. The interaction volume for generating X-rays is about 1 micron in diameter. More than 100 point analyses over bridgmanite-akimotoite grains and host glass regions show no apparent chemical variation. This is consistent with the hypothesis that the bridgmanite-bearing regions were orthopyroxene crystallites prior to shock and that bridgmanite and akimotoite formed from these pyroxenes during shock without significant chemical diffusion. Thus, we conclude that bridgmanite, co-existing akimotoite and host $(Mg,Fe)SiO_3$ glass have the same composition, within the error. Analytical results are given in Table S1.

Bridgmanite occurs as crystallites or crystalline aggregates, 50 – 400 nm in size, along with akimotoite in a $(Mg,Fe)SiO_3$ glass matrix (Figs. 1 and S1) as pseudomorphs of pyroxene clasts within a shock melt vein. Clinopyroxene with dominant diopside- and jadeite-components, ringwoodite, majorite, periclase, wadsleyite, troilite, and iron are present at other locations in the shock-melt vein. Olivine, enstatite and albitic glass are present in the wall rock portion of the sample.

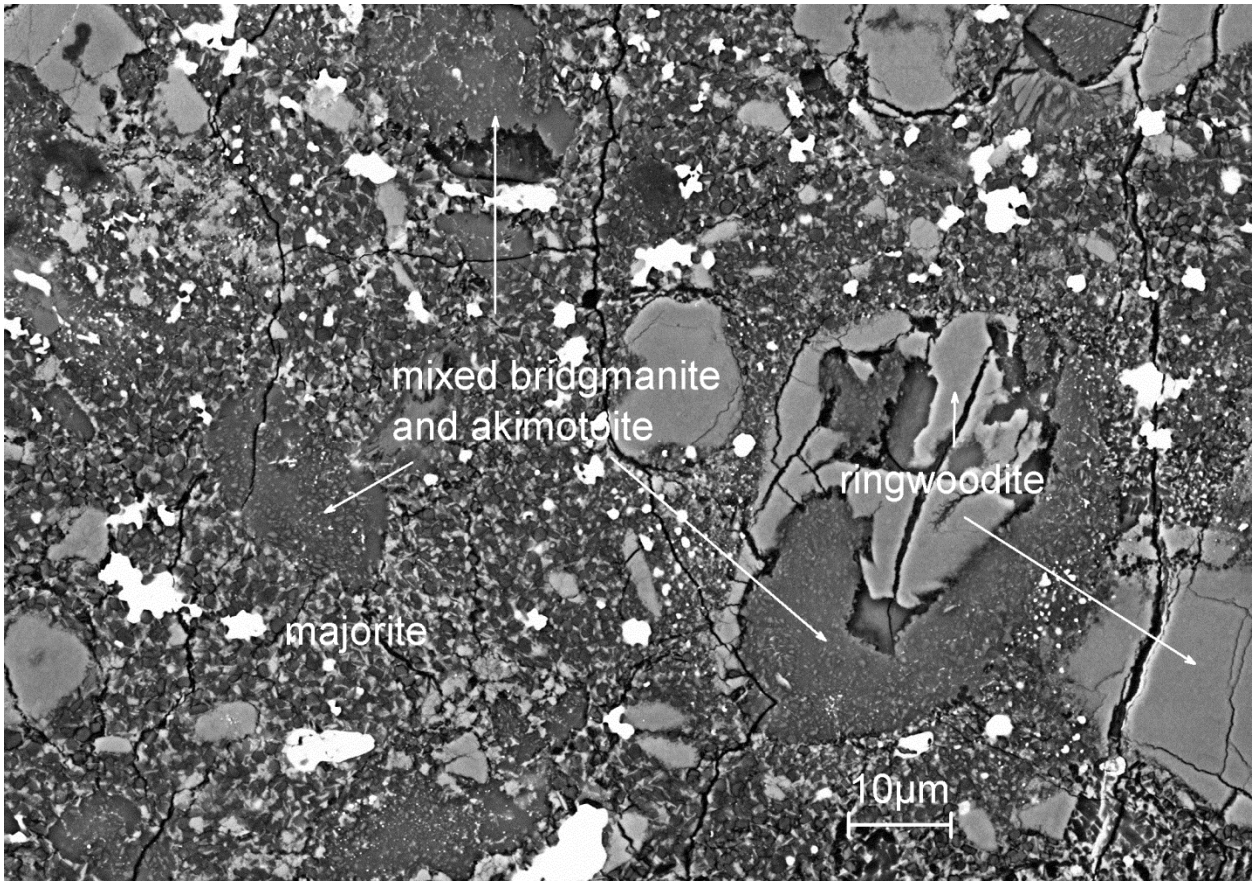

Fig. S1. Enlarged BSE image showing bridgmanite-akimotoite regions and surrounding phases**.** Bridgmanite-akimotoite aggregates as well as ringwoodite are pseudomorphs of pyroxene- and olivine clasts that were entrained in the shock melt vein.

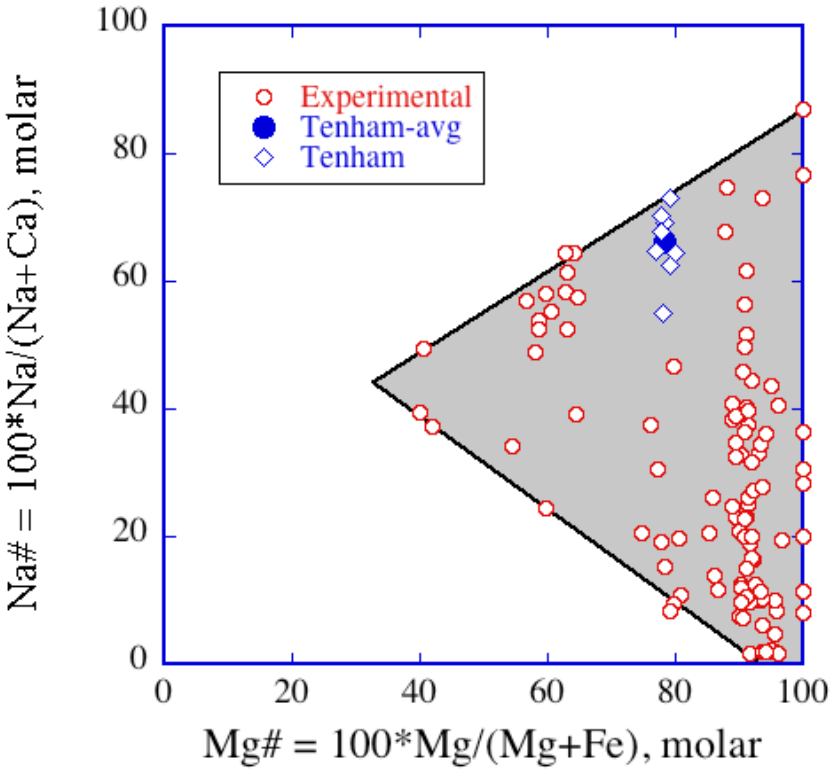

Fig. S2. Mg# (100*Mg/(Mg+Fe)) versus Na# (100*Na/(Na+Ca)) for natural and synthetic bridgmanite. Values are computed on a molar basis for bridgmanite from Tenham (this study for the type material) and experiments (*7,36-62*). The experimental data are multiply saturated and the black lines effectively denote solubility limits in bridgmanite for the bulk compositions studied. Compositions of the Tenham bridgmanites lie in a little bay of no experimental data but they are consistent with being near the experimentally expected solubility limit for Na-bearing bridgmanite with an Mg#~80.

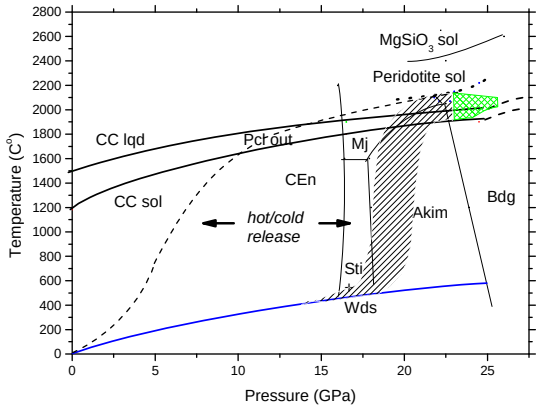

Fig. S3. Shock conditions for bridgmanite formation and the surrounding melt vein. Thin black lines indicate the phase diagram of $MgSiO_3$ (*63*). Thick lines: Solidus and liquidus for bulk Allende (*64*) as an approximation for metal-sulfide-peridotite melt mixtures. Thick dotted lines: Solidus of $MgSiO_3$ and peridotite (*36*). Blue curve: bulk rock adiabat. Green hashed field: Probable range of peak P-T conditions. The conditions of formation and recovery of bridgmanite in the shock melt vein are constrained by the observed occurrence of high pressure minerals, their paragenesis, and experimental constraints from phase diagrams and, generally, the cross-over of the free energies of phases even without common phase boundaries (*20*). Slopes of the cooling paths reflect a requirement that the initial release approximate the peak temperature adiabat, converge to the adiabat of the surrounding bulk rock at lower temperatures and, possibly, show a steep reduction of temperature at high pressure. Hot release is ultimately constrained by the disappearance of periclase as the liquidus phase at 8-10 GPa (*63*, *65*) and implies temperatures of 1600 to 2000 K within the high-pressure clinoenstatite stability field below 15 GPa or within the field for decomposition of bridgmanite to stishovite+wadsleyite between 16 and 18 GPa (*63*-*65*). Neither clinoenstatite nor the

breakdown products stishovite+wadsleyite were observed in vicinity of the akimotoite-bridgmanite aggregates. Hot- to intermediate-release is close to adiabatic between 20 and 25 GPa (*66*). The hot release limit is indicated by a dashed black curve. Cold release deviates from the 2200 K adiabat just below 22-23 GPa and temperature drops to below 1000 K, still within the field of akimotoite (grey hashed field). Peak pressures higher than 27 GPa imply rather hot release paths, as do temperatures above 2400K. Peak pressures above a 25-27 GPa margin imply release within the bridgmanite field and the possibility of crystallization from melt, which is not observed.

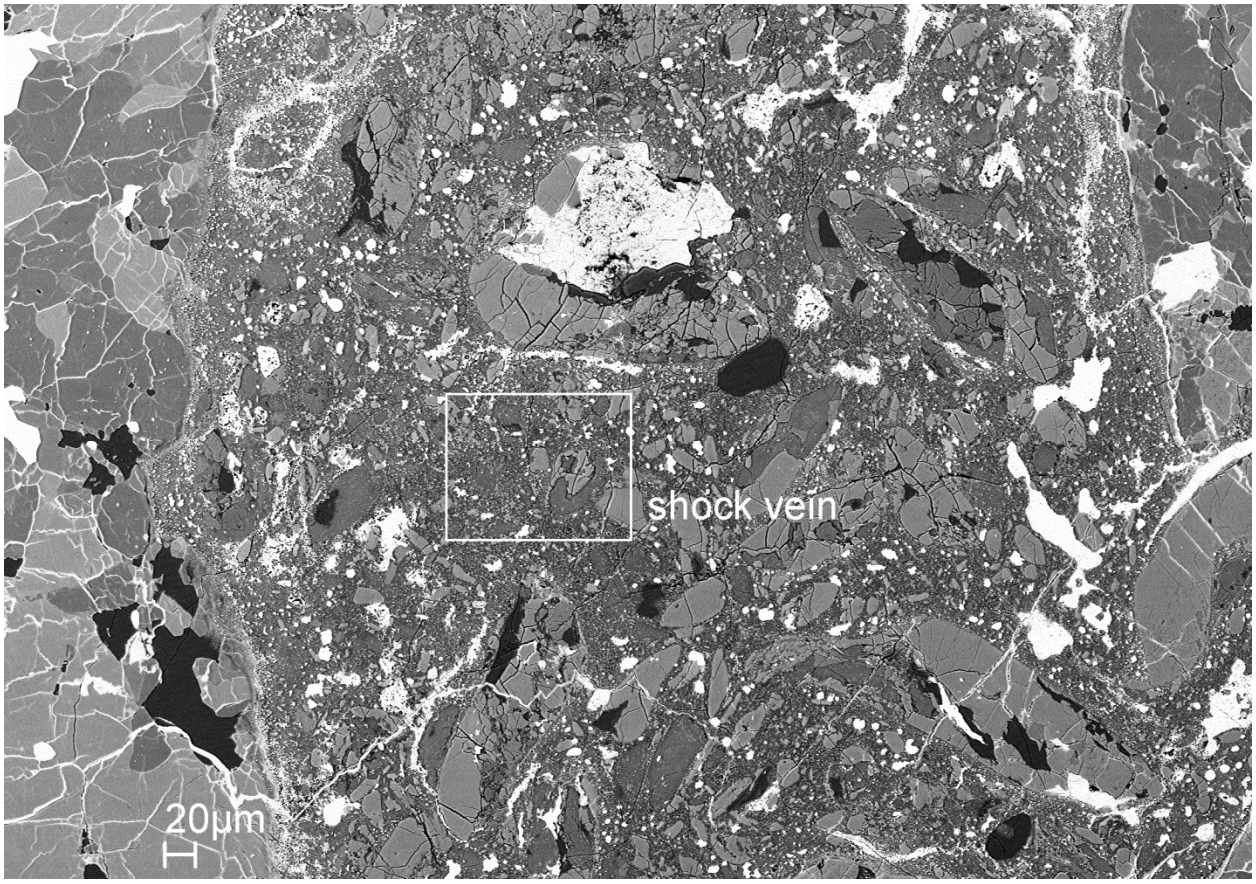

Fig. S4. SEM BSE image showing part of a shock melt vein in Tenham section USNM 7703. The rectangle marks where bridgmanite crystals were detected using a synchrotron micro-X-ray diffraction mapping.

Fig. S5. An optical image showing Tenham thin section USNM 7703 where bridgmanite was identified in a shock vein. The shock melt veins are dark brown to black over the thickness of the thin section of about 30 µm.

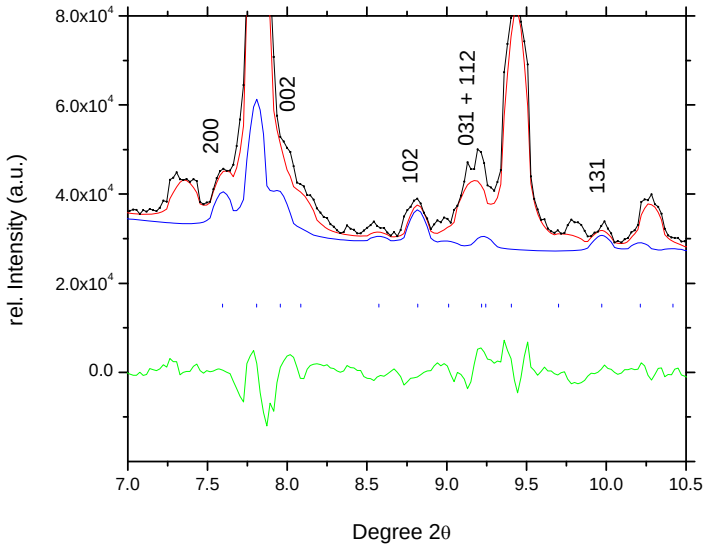
8.0x10^4
6.0x10^4
4.0x10^4
2.0x10^4
0.0
rel. Intensity (a.u.)
200
002
102
031 + 112
131
7.0
7.5
8.0
8.5
9.0
9.5
10.0
10.5
Degree 2θ

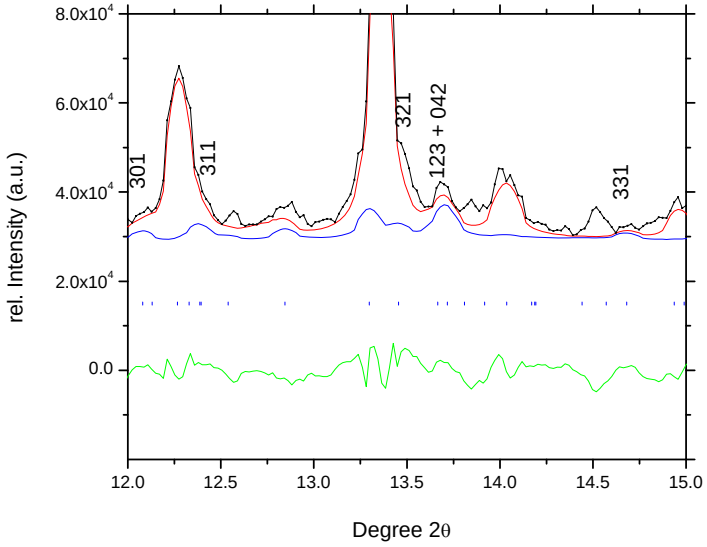
8.0x10^4
6.0x10^4
4.0x10^4
2.0x10^4
0.0
rel. Intensity (a.u.)
301
311
321
123 + 042
331
12.0
12.5
13.0
13.5
14.0
14.5
15.0
Degree 2θ

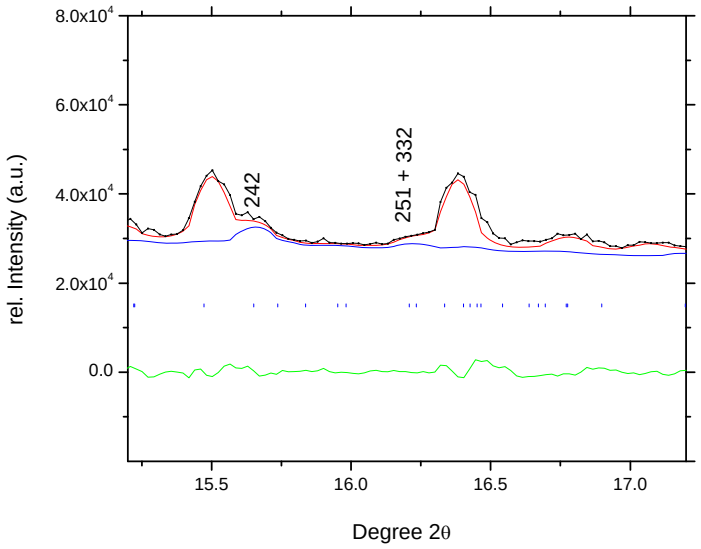

Fig. S 6a-c. Diffraction pattern zooms from Fig. 1. Strong reflections of bridgmanite are labeled by Miller indices. The overall quality of match between observed and calculated pattern is good (R_{wp} = 0.08), but the rather low volume fraction of bridgmanite (11 %) affects the fit of overlapping or weak reflections and R_{wp} is strongly weighted by the fit of the coexisting phases akimotoite and ringwoodite. Therefore, we extracted the apparent structure factor moduli of all reflections of bridgmanite from this fit and determined the R_{Bragg} to 0.15. This measure of goodness of fit reflects the overall level of match only of the bridgmanite fraction in the diffraction pattern. Because of the low volume fraction of bridgmanite, it is higher than the whole pattern Rietveld refinement parameter R_{wp}. Nevertheless, it shows that the assessment of bridgmanite structure and volume fraction is robust.

Table S1. Electron microprobe analytical results for bridgmanite and associated phases. The composition of akimotoite has been found identical to that of bridgmanite within uncertainties.

Constituent	bridgmanite	ringwoodite	majorite	maskelynite	Analytical Standard
(wt%)	n=7[a]	n=10	n=6	n=11	
SiO_2	55.6(0.3)[b]	38.5(0.3)	55(1)	68(1)	Anorthite
MgO	27.9(0.7)	36.7(0.9)	27.6(0.7)	0.02(0.01)	Forsterite
FeO	13.7(0.5)	25(1)	12.2(0.6)	0.35(0.04)	Fayalite
Na_2O	0.9(0.2)	b.d.[c]	1.4(0.2)	5(1)	Albite
CaO	0.9(0.2)	0.07(0.02)	1.2(0.5)	2.36(0.08)	Anorthite
MnO	0.49(0.03)	0.16(0.07)	0.52(0.08)	b.d.	Mn_2SiO_4
Al_2O_3	0.2(0.1)	b.d.	1(1)	22.6(0.2)	Anorthite
TiO_2	0.19(0.04)	b.d.	0.14(0.03)	0.05(0.02)	TiO_2
Cr_2O_3	0.13(0.02)	b.d.	0.15(0.05)	b.d.	Cr_2O_3
K_2O	0.04(0.03)	b.d.	0.10(0.02)	1.24(0.05)	Microcline
Total	100.1	100.4	99.3	99.6	

[a]n = number of analyses.

[b]Errors given inside parentheses are one standard deviation of the mean based on the n analyses.

[c]b.d.= below detection limit: 0.03 wt% Na, 0.04 wt% Al, 0.03 wt% Ti, 0.02 wt% K, 0.04 wt% Cr, 0.06 wt% Mn.

Table S2. Fractional atomic coordinates and site occupancies of bridgmanite. The unit cell of bridgmanite is a = 5.02± 0.03, b= 6.90± 0.03, and c = 4.81±0.02, all in Å, in space group 62, Pnma, with a volume of 167± 2 $Å^3$. We span the unit cell in the conventional first setting of space group 62 rather than the historically used third setting (Pbnm). The cif file is available as database S2.

	x/*a*	*y*/*b*	*z*/*c*	Occupancy	B_{iso}($Å^2$)
Mg 4c	0.557(2)	¼	0.513(3)	0.7(1)	0.43*
Fe 4c	0.557(2)	¼	0.513(3)	0.3(1)	0.43*
Si 4b	0	0	1/2	0.9 - 1.0	0.55*
Fe 4b	0	0	1/2	0.0 - 0.1	0.55*
O 4c	0.931(1)	1/4	0.381(3)	1	0.59*
O 8d	0.176(3)	0.575(1)	0.160(2)	1	0.39*

* B factors were not refined and are taken from two previous singe crystal structure analyses on synthetic material (*28*).

Data table s1 (Bridgmanite_hkl.xls) A list of observed and calculated factor moduli of Bridgmanite is available in data table S1. The observed moduli were obtained by LeBail-extraction from the powder diffraction pattern shown in Fig. 2. Multiplicities of the strictly overlapping reflections are given in this table. The calculated structure factor moduli are those of the final converged structure model obtained through global optimization (*35*). The primary beam wavelength was 0.3344 Å and the beam was 95% linear polarized. Miller indices are for the conventional first setting of space group 62.

References and Notes

1. L. Liu, Silicate perovskite from phase transformations of pyrope-garnet at high pressure and temperature. *Geophys. Res. Lett.* **1**, 277–280 (1974). doi:10.1029/GL001i006p00277

2. A. E. Ringwood, Phase transformations and their bearing on the constitution and dynamics of the mantle. *Geochim. Cosmochim. Acta* **55**, 2083–2110 (1991). doi:10.1016/0016-7037(91)90090-R

3. R. J. Hemley, R. E. Cohen, Silicate perovskite. *Annu. Rev. Earth Planet. Sci.* **20**, 553–600 (1992). doi:10.1146/annurev.ea.20.050192.003005

4. L. Stixrude, C. Lithgow-Bertelloni, Geophysics of chemical heterogeneity in the mantle. *Annu. Rev. Earth Planet. Sci.* **40**, 569–595 (2012). doi:10.1146/annurev.earth.36.031207.124244

5. E. Ito, E. Takahashi, Y. Matsui, The mineralogy and chemistry of the lower mantle: An implication of the ultrahigh-pressure phase-relations in the system MgO-FeO-SiO_2. *Earth Planet. Sci. Lett.* **67**, 238–248 (1984). doi:10.1016/0012-821X(84)90119-5

6. E. H. Nickel, J. D. Grice, The IMA commission on new minerals and mineral names: Procedures and guidelines on mineral nomenclature, 1998. *Can. Mineral.* **36**, 913–926 (1998).

7. M. Murakami, K. Hirose, N. Sata, Y. Ohishi, Post-perovskite phase transition and mineral chemistry in the pyrolitic lowermost mantle. *Geophys. Res. Lett.* **32**, L03304 (2005). 10.1029/2004GL021956 doi:10.1029/2004GL021956

8. L. Stixrude, C. Lithgow-Bertelloni, Thermodynamics of mantle minerals – II. Phase equiliobria. *Geophys. J. Int.* **184**, 1180–1213 (2011). doi:10.1111/j.1365-246X.2010.04890.x

9. D. J. Durben, G. H. Wolf, High-temperature behavior of metastable $MgSiO_3$ perovskite: A Raman-spectroscopic study. *Am. Minerol.* **77**, 890–893 (1992).

10. S. E. Kesson, J. D. Fitz Gerald, Partitioning of MgO, FeO, NiO, MnO and Cr_2O_3 between magnesian silicate perovskite and magnesiowüstite: Implications for the origin of inclusions in diamond and the composition of the lower mantle. *Earth Planet. Sci. Lett.* **111**, 229–240 (1992). doi:10.1016/0012-821X(92)90181-T

11. F. E. Brenker, T. Stachel, J. W. Harris, Exhumation of lower mantle inclusions in diamond: ATEM investigation of retrograde phase transitions, reactions and exsolution. *Earth Planet. Sci. Lett.* **198**, 1–9 (2002). doi:10.1016/S0012-821X(02)00514-9

12. R. A. Binns, R. J. Davis, S. J. B. Reed, Ringwoodite, natural $(Mg,Fe)_2SiO_4$ spinel in the Tenham meteorite. *Nature* **221**, 943–944 (1969). doi:10.1038/221943a0

13. J. V. Smith, B. Mason, Pyroxene-garnet transformation in coorara meteorite. *Science* **168**, 832–833 (1970). Medline doi:10.1126/science.168.3933.832

14. G. D. Price, A. Putnis, S. O. Agrell, D. G. W. Smith, Wadsleyite, natural β-$(Mg,Fe)_2SiO_4$ from the Peace River meteorite. *Can. Min.* **21**, 29–35 (1983).

15. N. Tomioka, K. Fujino, Akimotoite, $(Mg,Fe)SiO_3$, a new silicate mineral of the ilmenite group in the Tenham chondrite. *Am. Minerol.* **84**, 267–271 (1999).

16. T. G. Sharp, C. M. Lingemann, C. Dupas, D. Stöffler, Natural occurrence of $MgSiO_3$-ilmenite and evidence for $MgSiO_3$-perovskite in a shocked L chondrite. *Science* **277**, 352–355 (1997). doi:10.1126/science.277.5324.352

17. H. Mori, Shock-induced phase transformations of the Earth and planetary materials. *J. Minerol. Soc. Japan* **23**, 171–178 (1994).

18. N. Miyajima, A. E. Goresy, C. Dupas-Bruzek, F. Seifert, D. C. Rubie, M. Chen, X. Xie, Ferric iron in Al-bearing akimotoite coexisting with iron-nickel metal in a shock-melt vein in an L-6 chondrite. *Am. Minerol.* **92**, 1545–1549 (2007). doi:10.2138/am.2007.2546

19. M. Miyahara, E. Ohtani, S. Ozawa, M. Kimura, A. El Goresy, T. Sakai, T. Nagase, K. Hiraga, N. Hirao, Y. Ohishi, Natural dissociation of olivine to $(Mg,Fe)SiO_3$ perovskite and magnesiowustite in a shocked Martian meteorite. *Proc. Natl. Acad. Sci. U.S.A.* **108**, 5999–6003 (2011). Medline doi:10.1073/pnas.1016921108

20. Z. D. Xie, T. G. Sharp, P. S. DeCarli, High-pressure phases in a shock-induced melt vein of the Tenham L6 chondrite: Constraints on shock pressure and duration. *Geochim. Cosmochim. Acta* **70**, 504–515 (2006). doi:10.1016/j.gca.2005.09.003

21. S.-N. Luo, J. A. Akins, T. J. Ahrens, P. D. Asimow, Shock-compressed $MgSiO_3$ glass, enstatite, olivine, and quartz: Optical emission, temperatures, and melting. *J. Geophys. Res.* **109** (B5), B05205 (2004). 10.1029/2003JB002860 doi:10.1029/2003JB002860

22. C. Sanchez-Valle, J. D. Bass, Elasticity and pressure-induced structural changes in vitreous $MgSiO_3$-enstatite to lower mantle pressures. *Earth Planet. Sci. Lett.* **295**, 523–530 (2010). doi:10.1016/j.epsl.2010.04.034

23. See the supplementary materials.

24. D. R. Hummer, Y. W. Fei, Synthesis and crystal chemistry of Fe^{3+}-bearing $(Mg,Fe^{3+})(Si,Fe^{3+})O_3$ perovskite. *Am. Minerol.* **97**, 1915–1921 (2012). doi:10.2138/am.2012.4144

25. B. Grocholski, K. Catalli, S.-H. Shim, V. Prakapenka, Mineralogical effects on the detectability of the postperovskite boundary. *Proc. Natl. Acad. Sci. U.S.A.* **109**, 2275–2279 (2012). Medline doi:10.1073/pnas.1109204109

26. H. Y. McSween Jr., T. C. Labotka, Oxidation during metamorphism of the ordinary chondrites. *Geochim. Cosmochim. Acta* **57**, 1105–1114 (1993). doi:10.1016/0016-7037(93)90044-W

27. C. M. Bertka, Y. Fei, Mineralogy of the Martian interior up to core-mantle boundary pressures. *J. Geophys. Res.* **102**, 5251–5264 (1997). doi:10.1029/96JB03270

28. A. P. Hammersley, S. O. Svensson, M. Hanfland, A. N. Fitch, D. Hausermann, Two-dimensional detector software: From real detector to idealised image or two-theta scan. *High Press. Res.* **14**, 235–248 (1996). doi:10.1080/08957959608201408

29. P. Dera et al., High pressure single-crystal micro X-ray diffraction analysis with GSE_ADA/RSV software. *High Pressure Res.* **33** (special issue), 466–484 (2013).

30. W. Kraus, G. Nolze, POWDER CELL – a program for the representation and manipulation of crystal structures and calculation of the resulting X-ray powder patterns. *J. Appl. Cryst.* **29**, 301–303 (1996). doi:10.1107/S0021889895014920

31. H. Putz, J. C. Schön, M. Jansen, Combined method for *ab initio* structure solution from powder diffraction data. *J. Appl. Cryst.* **32**, 864–870 (1999). doi:10.1107/S0021889899006615

32. R. G. Trønnes, D. J. Frost, Peridotite melting and mineral-melt partitioning of major and minor elements at 22-24.5 GPa. *Earth Planet. Sci. Lett.* **197**, 117–131 (2002). doi:10.1016/S0012-821X(02)00466-1

33. Y. Asahara, T. Kubo, T. Kondo, Phase relations of a carbonaceous chondrite at lower mantle conditions. *Phys. Earth Planet. Inter.* **143-144**, 421–432 (2004). doi:10.1016/j.pepi.2003.10.011

34. M. Chen, A. El Goresy, D. Frost, P. Gillet, Melting experiments of a chondritic meteorite between 16 and 25 GPa: Implication for Na/K fractionation in a primitive chondritic Earth's mantle. *Eur. J. Min* **16**, 203–211 (2004). doi:10.1127/0935-1221/2004/0016-0203

35. A. Corgne, C. Liebske, B. J. Wood, D. C. Rubie, D. J. Frost, Silicate perovskite-melt partitioning of trace elements and geochemical signature of a deep perovskitic reservoir. *Geochim. Cosmochim. Acta* **69**, 485–496 (2005). doi:10.1016/j.gca.2004.06.041

36. C. Dalou, K. T. Koga, T. Hammouda, F. Poitrasson, Trace element partitioning between carbonatitic melts and mantle transition zone minerals: Implications for the source of carbonatites. *Geochim. Cosmochim. Acta* **73**, 239–255 (2009). doi:10.1016/j.gca.2008.09.020

37. K. Hirose, Phase transitions in pyrolitic mantle around 670-km depth: Implications for upwelling of plumes from the lower mantle. *J. Geophys. Res.* **107**, 2078 (2002). 10.1029/2001JB000597 doi:10.1029/2001JB000597

38. K. Hirose, Y. Fei, Subsolidus and melting phase relations of basaltic composition in the uppermost lower mantle. *Geochim. Cosmochim. Acta* **66**, 2099–2108 (2002). doi:10.1016/S0016-7037(02)00847-5

39. K. Hirose, N. Shimizu, W. van Westrenen, Y. Fei, Trace element partitioning in Earth's lower mantle and implications for geochemical consequences of partial melting at the core-mantle boundary. *Phys. Earth Planet. Inter.* **146**, 249–260 (2004). doi:10.1016/j.pepi.2002.11.001

40. T. Irifune, T. Shinmei, C. A. McCammon, N. Miyajima, D. C. Rubie, D. J. Frost, Iron partitioning and density changes of pyrolite in Earth's lower mantle. *Science* **327**, 193–195 (2010). Medline doi:10.1126/science.1181443

41. T. Ishii, H. Kojitani, M. Akaogi, Post-spinel transitions in pyrolite and Mg_2SiO4 and akimotoite-perovskite transition in $MgSiO_3$: Precise comparison by high-pressure high-temperature experiments with multi-sample cell technique. *Earth Planet. Sci. Lett.* **309**, 185–197 (2011). doi:10.1016/j.epsl.2011.06.023

42. C. Kato, K. Hirose, T. Komabayashi, H. Ozawa, Y. Ohishi, NAL phase in K-rich portions of the lower mantle. *Geophys. Res. Lett.* **40**, 5085–5088 (2013). doi:10.1002/grl.50966

43. C. Liebske, A. Corgne, D. J. Frost, D. C. Rubie, B. J. Wood, Compositional effects on element partitioning between Mg-silicate perovskite and silicate melts. *Contrib. Mineral. Petrol.* **149**, 113–128 (2005). doi:10.1007/s00410-004-0641-8

44. K. D. Litasov, E. Ohtani, Phase relations in hydrous MORB at 18-28 GPa: Implications for heterogeneity of the lower mantle. *Phys. Earth Planet. Inter.* **150**, 239–263 (2005). doi:10.1016/j.pepi.2004.10.010

45. K. D. Litasov, E. Ohtani, Solidus and phase relations of carbonated peridotite in the system CaO-Al_2O_3-MgO-SiO_2-Na_2O-CO_2 to the lower mantle depths. *Phys. Earth Planet. Inter.* **177**, 46–58 (2009). doi:10.1016/j.pepi.2009.07.008

46. K. D. Litasov, E. Ohtani, The solidus of carbonated eclogite in the system CaO-Al_2O_3-MgO-SiO_2-Na_2O-CO_2 to 32 GPa and carbonatite liquid in the deep mantle. *Earth Planet. Sci. Lett.* **295**, 115–126 (2010). doi:10.1016/j.epsl.2010.03.030

47. C. A. McCammon, S. Lauterbach, F. Seifert, F. Langenhorst, P. A. van Aken, Iron oxidation state in lower mantle mineral assemblages I. Empiricial relations derived from high-pressure experiments. *Earth Planet. Sci. Lett.* **222**, 435–449 (2004). doi:10.1016/j.epsl.2004.03.018

48. E. A. McFarlane, M. J. Drake, D. C. Rubie, Element partitioning between Mg-perovskite, magnesiowüstite, and silicate melt at conditions of the Earth's mantle. *Geochim. Cosmochim. Acta* **58**, 5161–5172 (1994). doi:10.1016/0016-7037(94)90301-8

49. Y. Nishihara, E. Takahashi, Phase relation and physical properties of an Al-depleted komatiite to 23 GPa. *Earth Planet. Sci. Lett.* **190**, 65–77 (2001). doi:10.1016/S0012-821X(01)00378-8

50. N. Nishiyama, T. Yagi, Phase relation and mineral chemistry in pyrolite to 2200°C under lower mantle pressures and implications for dynamics of mantle plumes. *J. Geophys. Res.* **108**, 2255 (2003). 10.1029/2002JB002216 doi:10.1029/2002JB002216

51. N. Nishiyama, T. Irifune, T. Inoue, J.- Ando, K.- Funakoshi, Precise determination of phase relations in pyrolite across the 660 km seismic discontinuity by in situ X-ray diffraction and quench experiments. *Phys. Earth Planet. Inter.* **143-144**, 185–199 (2004). doi:10.1016/j.pepi.2003.08.010

52. S. Ono, E. Ito, T. Katsura, Mineralogy of subducted basaltic crust (MORB) from 25 to 37 GPa, and chemical heterogeneity of the lower mantle. *Earth Planet. Sci. Lett.* **190**, 57–63 (2001). doi:10.1016/S0012-821X(01)00375-2

53. A. Ricolleau, G. Fiquet, A. Addad, N. Menguy, C. Vanni, J.-P. Perrillat, I. Daniel, H. Cardon, N. Guignot, Analytical transmission electron microscopy study of a natural MORB sample assemblage transformed at high pressure and high temperature. *Am. Minerol.* **93**, 144–153 (2008). doi:10.2138/am.2008.2532

54. T. Sanehira, T. Irifune, T. Shinmei, H. Ohfuji, F. Brunet, K.-I. Funakoshi, Density profiles of pyrolite and MORB compositions across the 660 km seismic discontinuity. *High Press. Res.* **28**, 335–349 (2008). doi:10.1080/08957950802251357

55. A. Sano, E. Ohtani, K. Litasov, T. Kubo, T. Hosoya, K. Funakoshi, T. Kikegawa, In situ X-ray diffraction study of the effect of water on the garnet-perovskite transformation in

MORB and implications for the penetration of oceanic crust into the lower mantle. *Phys. Earth Planet. Inter.* **159**, 118–126 (2006). doi:10.1016/j.pepi.2006.07.004

56. H. Taura, H. Yurimoto, T. Kato, S. Sueno, Trace element partitioning between silicate perovskites and ultracalcic melt. *Phys. Earth Planet. Inter.* **124**, 25–32 (2001). doi:10.1016/S0031-9201(00)00221-1

57. M. J. Walter, E. Nakamura, R. G. Trønnes, D. J. Frost, Experimental constraints on crystallization differentiation in a deep magma ocean. *Geochim. Cosmochim. Acta* **68**, 4267–4284 (2004). doi:10.1016/j.gca.2004.03.014

58. B. J. Wood, Phase transformations and partitioning relations in peridotite under lower mantle conditions. *Earth Planet. Sci. Lett.* **174**, 341–354 (2000). doi:10.1016/S0012-821X(99)00273-3

59. Y. Tange, E. Takahashi, Y. Nishihara, K.- Funakoshi, N. Sata, Phase relations in the system MgO-FeO-SiO_2 to 50 GPa and 2000°C: An application of experimental techniques using multianvil apparatus with sintered diamond anvils. *J. Geophys. Res.* **114** (B2), B02214 (2009). 10.1029/2008JB005891 doi:10.1029/2008JB005891

60. C. B. Agee, J. Li, M. C. Shannon, S. Circone, Pressure-temperature phase diagram for the Allende meteorite. *J. Geophys. Res. Solid Earth* **100**, 17725–17740 (1995). doi:10.1029/95JB00049

61. E. Ohtani, K. Moriwaki, T. Kato, K. Onuma, Melting and crystal-liquid partitioning in the system Mg_2SiO_4-Fe_2SiO_4 to 25 GPa. *Phys. Earth Planet. Inter.* **107**, 75–82 (1998). doi:10.1016/S0031-9201(97)00125-8

62. C. W. Thomas, Q. Liu, C. B. Agee, P. D. Asimow, R. A. Lange, Multi-technique equation of state for Fe_2SiO_4 melt and the density of Fe-bearing silicate melts from 0 to 161 GPa. *J. Geophys. Res. Solid Earth* **117**, B10206 (2012). doi:10.1029/2012JB009403

63. K. Catalli, S.-H. Shim, V. B. Prakapenka, J. Zhao, W. Sturhahn, P. Chow, Y. Xiao, H. Liu, H. Cynn, W. J. Evans, Spin state of ferric iron in $MgSiO_3$ perovskite and its effect on elastic properties. *Earth Planet. Sci. Lett.* **289**, 68–75 (2010). doi:10.1016/j.epsl.2009.10.029

64. T. B. Ballaran, A. Kurnosov, K. Glazyrin, D. J. Frost, M. Merlini, M. Hanfland, R. Caracas, Effect of chemistry on the compressibility of silicate perovskite in the lower mantle. *Earth Planet. Sci. Lett.* **333-334**, 181–190 (2012). doi:10.1016/j.epsl.2012.03.029

65. C. B. Vanpeteghem, J. Zhao, R. J. Angel, N. L. Ross, N. Bolfan-Casanova, Crystal structure and equation of state of $MgSiO_3$ perovskite. *Geophys. Res. Lett.* **33**, L03306 (2006). doi:10.1029/2005GL024955

66. Y. Kudoh, C. T. Prewitt, L. W. Finger, A. Darovskikh, E. Ito, Effect of iron on the crystal-structure of $(Mg,Fe)SiO_3$ perovskite. *Geophys. Res. Lett.* **17**, 1481–1484 (1990). doi:10.1029/GL017i010p01481